

Extremely late photometry of the nearby SN 2011fe^{*}

W. E. Kerzendorf,¹ C. McCully,^{2,3} S. Taubenberger,¹ A. Jerkstrand,⁴ I. Seitenzahl,^{5,6,7}
A. J. Ruiter,^{6,7,5} J. Spyromilio,¹, K. S. Long^{8,9} and C. Fransson¹⁰

¹European Southern Observatory, Karl-Schwarzschild-Str. 2, 85748 Garching bei München, Germany

²Department of Physics, University of California, Santa Barbara, Broida Hall, Mail Code 9530, Santa Barbara, CA 93106-9530, USA

³Las Cumbres Observatory, Global Telescope Network, 6740 Cortona Drive Suite 102, Goleta, CA 93117, USA

⁴Max Planck Institute for Astrophysics, Garching bei München, Karl-Schwarzschild-Str. 1, Postfach 1317, D-85741 Garching, Germany

⁵School of Physical, Environmental and Mathematical Sciences, University of New South Wales, Australian Defence Force Academy, Canberra, ACT 2600, Australia

⁶Research School of Astronomy and Astrophysics, Australian National University, Canberra, ACT 0200, Australia

⁷ARC Centre of Excellence for All-sky Astrophysics (CAASTRO)

⁸Space Telescope Science Institute, 3700 San Martin Drive, Baltimore, MD, 21218, USA

⁹Eureka Scientific, Inc. 2452 Delmer Street, Suite 100, Oakland, CA 94602-3017

¹⁰Department of Astronomy, The Oskar Klein Centre, Stockholm University, Alba Nova University Centre, SE-106 91 Stockholm, Sweden

8 October 2018

ABSTRACT

Type Ia supernovae are widely accepted to be the outcomes of thermonuclear explosions in white dwarf stars. However, many details of these explosions remain uncertain (e.g. the mass, ignition mechanism, and flame speed). Theory predicts that at very late times (beyond 1000 d) it might be possible to distinguish between explosion models. Few very nearby supernovae can be observed that long after the explosion. The Type Ia supernova SN 2011fe located in M101 and along a line of sight with negligible extinction, provides us with the once-in-a-lifetime chance to obtain measurements that may distinguish between theoretical models. In this work, we present the analysis of photometric data of SN 2011fe taken between 900 and 1600 days after explosion with Gemini and *HST*. At these extremely late epochs theory suggests that the light curve shape might be used to measure isotopic abundances which is a useful model discriminant. However, we show in this work that there are several currently not well constrained physical processes introducing large systematic uncertainties to the isotopic abundance measurement. We conclude that without further detailed knowledge of the physical processes at this late stage one cannot reliably exclude any models on the basis of this dataset.

Key words: supernovae: individual: (SN 2011fe) – nuclear reactions, nucleosynthesis, abundances – techniques: photometric

1 INTRODUCTION

Type Ia supernovae (SNe Ia) have been very successful distance indicators partially due to the fact that they form a relatively homogeneous class.

Specifically, this homogeneity is driven by the fact that the majority of the radiated energy is provided by the decay chain $^{56}\text{Ni} \rightarrow ^{56}\text{Co} \rightarrow ^{56}\text{Fe}$ (Colgate & McKee 1969). The energy is released in γ -rays and positrons that interact through Compton scattering and deposit their energy in heating the free electron gas, ionisations and excitations. This isotope chain, the lack of hydrogen, and existence of intermediate mass elements point to explosive nucleosynthesis in highly degenerate matter present in massive CO white dwarfs ($1 M_{\odot} - 1.4 M_{\odot}$). However, the precise mass

range, ignition mechanism and flame propagation (deflagration, detonation, mixed scenarios) remain to be discovered.

In this work, we will focus on two specific models: The traditional scenario that sees the self-ignition of a CO white dwarf at a mass of $\approx 1.38 M_{\odot}$ (known as Chandrasekhar mass models) and alternate scenarios that ignite mostly due to dynamical effects (such as mergers). Röpke et al. (2012) presents two representatives of these two classes: A model at $1.38 M_{\odot}$ (N100) and a violent merger of a $0.9 M_{\odot}$ and $1.1 M_{\odot}$ CO white dwarfs. Both scenarios result in similar observables due to the comparable amounts of ^{56}Ni produced and thus are not easily distinguishable.

Specifically, both the models are currently able to produce synthetic light curves and spectra that are consistent with early epoch observations of SNe Ia (≈ 30 days post-

explosion; e.g. Röpke et al. 2012). Thus early time observations can not be easily used to successfully discriminate between the competing scenarios. However, late time photometry (from a few hundred days onwards) may provide an avenue to determine the progenitor system.

One of the main difference between the two models is the density at which a large fraction of the matter burns ($> 2 \times 10^8 \text{ g cm}^{-3}$ for the N100 model and $< 2 \times 10^8 \text{ g cm}^{-3}$ for the merger model). Both models produce similar amounts of ^{56}Ni but the ^{57}Ni and ^{55}Co yields are different for these two channels. This effect can be seen in very late light curves $\gtrsim 1000 \text{ d}$ when their daughter nuclei (^{57}Co and ^{55}Fe) start to dominate the energy deposition (Seitenzahl et al. 2009; Seitenzahl 2011). This difference leads to a slower decline of the light curve of the N100 model compared to the merger scenario at epochs $\gtrsim 1000 \text{ d}$ (Röpke et al. 2012). However, at these late times the supernova is roughly a million times dimmer than at peak and thus this experiment can only be performed on very close-by objects.

SN 2011fe is one of the closest SNe Ia (6.4 Mpc; Shappee & Stanek 2011) and is essentially unattenuated ($A_V < 0.05$; Patat et al. 2013). It provides us with a unique opportunity to observe a spectroscopically ‘normal’ SN Ia later than any other SN Ia (for a detailed description of SN 2011fe see Shappee et al. 2017), thus allowing us to test the predicted difference in light curve shapes at very late epochs.

We note that Shappee et al. (2017) and Dimitriadis et al. (2017) have used datasets that overlap with those used in this work but have drawn different conclusions on the progenitor system despite using similar methods. This is due to the different treatment of the systematic uncertainties that affect the late light curve modelling – a particular focus of this work (these systematics might affect similar studies on other supernovae; e.g. SN 2012cg and SN 2014J. Graur et al. 2016; Yang et al. 2017).

The method is fundamentally simple: Assuming that the energy that is measured (in this case between 0.4 – 1.6 micron) is proportional to the energy produced by the decay of the important isotopes ^{56}Ni , ^{57}Ni , and ^{55}Co , we can infer the presence and amount of these isotopes in the ejecta. The complication in the experiment is to determine the systematic effects that affect the proportionality of the amounts of the isotopes to the observed flux (c.f. Milne et al. 2001).

There are several such effects that might lead to a deviation between UV/optical/Near-IR (UVOIR) flux and the radioactively injected energy at very late times. Shappee et al. (2017); Dimitriadis et al. (2017) already discuss several possibilities (surviving companion, light echoes, CSM interactions) and suggest that none of these do contribute significant flux for this supernova.

In this paper, we will focus on effects that are closely related to the decay radiation. Fast electrons and positrons are a crucial energy carriers at these late times. Chan & Lingenfelter (1993) suggested that some of these energy carriers (positrons) may begin to escape from the SN without annihilating as early as a few hundred days after explosion, resulting in a departure from the exponential decline (discussed in detail in Kerzendorf et al. 2014). While some authors (e.g. Milne et al. 1999, 2001) argue for moderate positron escape occurring in some SNe Ia, more recent publications that take essential near-IR corrections into account require almost complete trapping of positrons up to quite

late epochs to explain observations (e.g. Sollerman et al. 2004; Stritzinger & Sollerman 2007; Leloudas et al. 2009). This complete trapping can be explained by a tangled magnetic field, which in turn could be used to constrain the nature of the progenitor white dwarf.

Axelrod (1980) predicted that the optical and near-IR light curves will decline much more rapidly after $\sim 700 \text{ d}$, even if all positrons remain trapped due to an infrared catastrophe (IRC). The IRC is predicted to occur when the electron gas temperature drops below that required to collisionally excite optical and near-IR atomic transitions ($T \lesssim 1500 \text{ K}$), and cooling proceeds only via fine structure lines emitting in the far-IR. This cooling is constant while the energy input continues to decline exponentially. In Spyromilio & Graham (1992), the IRC was determined to have occurred in the core-collapse SN 1987A. However, such a dimming has never been observed for SNe Ia (e.g. Leloudas et al. 2009) which remains a puzzle for late time light curves.

Fransson & Jerkstrand (2015) suggest that while a large fraction of the energy is radiated away by fine structure lines in the far-IR, the observed flux in the UVOIR bands comes from non-thermal excitation of Fe that produces UV photons, which in turn interact with the ejecta and produce the observed flux distribution.

In this work, we expand the previous observational data set on SN 2011fe and use a Bayesian framework to be able to incorporate prior knowledge quantitatively into the analysis process to give a consistent measurement of the isotopic ratios.

In Section 2 we present our observations. In Section 3 we discuss the analysis – specifically the construction of the quasi-bolometric light curve and the light curve model. We discuss the various physical processes that lead to systematic uncertainties in Section 4 and conclude the paper in Section 5.

2 OBSERVATIONS

2.1 HST Photometry

The observations presented in this work are compiled from three different programs (PI: Kerzendorf – GO 13824; PI: Shappee – GO 14166, GO 13737) which imaged SN 2011fe ($\alpha = 14^{\text{h}}03^{\text{m}}05^{\text{s}}.7$, $\delta = +54^{\circ}16'25.18''$) between 1125 and 1623 d after $\text{MJD}_{\text{max}} = 55814.51$ (Pereira et al. 2013) using both Wide-Field Camera 3 (WFC3) and Advanced Camera for Surveys (ACS). In addition, we have included archival ACS observations from GO 9490 (PI: Kuntz).

We generally use the ‘‘FLC’’ frames with charge transfer efficiency (CTE; see Chiaberge et al. 2009, for a description) correction throughout our work. For sub-frame images (our UVIS WFC3 images) could not be CTE corrected. The systematics introduced by this are negligible as SN 2011fe is located very close to the amplifier.

We did coarse registration of our single frames with our registered templates. For this step, we used ASTROSCRAPPY¹ to clean the raw frames to improve the matching process. We then selected the 120 brightest stars around

¹ <https://github.com/astropy/astroscrappy> (cf. van Dokkum 2001)

SN 2011fe and matched those to stars in the reference image (Visit 4 - F438W drizzled frame). We then fit a TAN-projection WCS matrix (four parameters) transforming between the image coordinates of the stars within the unregistered frame and the WCS coordinates in the new frame using the differential evolution algorithm (implemented in `SCIPY.OPTIMIZE.DIFFERENTIAL_EVOLUTION`). The registered images produced from this technique had a median offset ≈ 0.1 pixel for each of the matching stars.

We then did a fine registration using the TWEAKREG algorithm before we combined frames. The final cosmic ray rejection was done on raw FLC frames and thus combined the dithered observations using `ASTRODRIZZLE` (Gonzaga & et al. 2012) (combining frames that come from the same visit, instrument and filter).

We ran `DOLPHOT` (Dolphin 2000) – a PSF photometry package – on all images: `DOLPHOT` runs on the individual frames, but registers to a template drizzled frame; photometry is performed on all frames simultaneously. For a source to be detected it must be detected at least in one frame with a $2.5\text{-}\sigma$ threshold or on the combined with a $3.5\text{-}\sigma$ threshold. If a source is detected it is added to the catalogue and PSF photometry is performed in this position on all frames. For this the frames must be astrometrically matched. This technique allows us to extract the most accurate photometry for the supernova even in images where nearby stars are close to it.

On the resulting catalogue we performed a standard cut of object type (1, 2 as described in the `DOLPHOT` manual), in sharpness between -0.3 and 0.3 as well as crowding < 0.5 .

We then produced the final photometry for each star by combining the individual measurements using standard uncertainty propagation.

As reported in Shappee et al. (2015) crowding is an issue for this source in the infrared bands (see Figure 1). However fitting photometry for SN 2011fe on all frames simultaneously allows us to extract stellar photometry also for the under-resolved regions in the infrared WFC3 images. We have checked the magnitudes of nearby stars to ensure that the flux of these remains constant over time and thus do not contribute to the supernova measurement.

We verified the `DOLPHOT` uncertainties by checking the scatter of flux measurements of 1073 stars around the supernova. The results show that `DOLPHOT` often overestimated the uncertainty by a factor of 1.5 (in roughly 2/3 of the cases) or are close to the uncertainty. This suggests that the uncertainty determination is reliable.

For two of our measurements the uncertainties are of similar magnitude as the measurements themselves (indicated in the table). We used three times this uncertainty and treated this as an upper limit. In all future processing, the bounded errors are treated as being normally distributed while the upper limits are treated as having uniform probability distributions between $[0, \text{upper limit}]$.

The final photometry for SN 2011fe is shown in Table 1 and the synthetic evolving SED is shown in Figure 2.

2.2 Gemini Photometry

We obtained multicolour photometry using GMOS (Gemini Multi Object Spectrograph; Hook et al. 2004) mounted on the Gemini North telescope. Images were taken in the g ,

r , i , and z bands under the program GN-2014A-Q-24. The first epoch (nights of 2014 March 7, 27, and 28) has already been published by Kerzendorf et al. (2014), while the second epoch (night of 2014 June 27) is presented here.

The data were pre-reduced with the `GEMINIUTIL`² package following standard procedures. After careful inspection of the world coordinate system, the images were aligned and combined using `SWARP` (Bertin et al. 2002). In a final step, we adjusted the astrometric calibration to match ACS observations. We undertook the same operations on SDSS-calibrated stars (Aihara et al. 2011) in the field and then used those for the calibration.

Subsequently, we performed our measurements using point-spread function (PSF) photometry with the `SNOOPY` package. This package is a compilation of `IRAF`³ tasks optimized for supernova (SN) photometry, developed by F. Patat and E. Cappellaro. `SNOOPY` constructs the PSF by selecting several clean unblended stars and then performs PSF photometry on the SN itself. The instrumental SN magnitudes were finally calibrated to the Sloan photometric system (Fukugita et al. 1996) using tabulated atmospheric extinction coefficients and the nightly zero points derived from our standard-field observations.

To get a better estimate of the uncertainty of the photometric measurement, `SNOOPY` uses an artificial star experiment.

3 ANALYSIS

Our analysis consists of three distinct actions. First we combine the individual photometric measurements, reconstructing a quasi-bolometric flux that is comparable cross-epoch (despite the use of different filter sets - see Figure 3). Then we construct a light curve model with various options and finally we explore the parameter space of the model given our observed data.

3.1 Reconstructing a quasi-bolometric flux

For our analysis we compare the complete flux emerging in the UVOIR bands with the energy produced by radioactive decay. Thus we aimed to create a measure of this UVOIR flux that is consistent across all epochs (and taking into account filter overlap). To do this we scale a synthetic spectrum to our observed photometry and use the integrated flux of this spectrum for our comparison (using the nomenclature and technique of Shappee et al. 2017, aptly named quasi-bolometric flux). We only have one measurement in the U band (F336W) and thus we exclude this band from the reconstruction as our main goal is to explore the flux evolution.

Fransson & Jerkstrand (2015) have modeled the physical processes and published a synthetic spectrum for SN 2011fe around 1000 days past explosion that is ideal

² <http://github.com/geminiutil/geminiutil>

³ `IRAF`: the Image Reduction and Analysis Facility is distributed by the National Optical Astronomy Observatory, which is operated by the Association of Universities for Research in Astronomy (AURA) under cooperative agreement with the National Science Foundation (NSF).

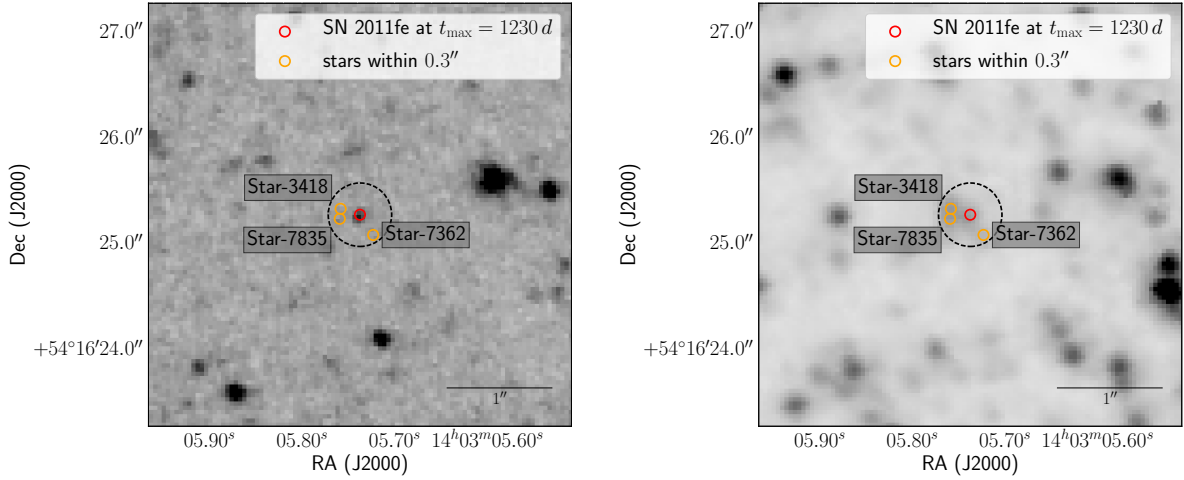


Figure 1. Left: HST ACS F475W image of SN 2011fe at 1230 d past maximum. Right: HST WFC3 F160W image at 1230 d past maximum. Sources within a circle of 0.3 arcsec radius around SN 2011fe are marked.

Table 1. Photometry for SN 2011fe.

Visit ID	t_{\max} [d]	Instrument	Filter	t_{\exp} [s]	exposures	flux [$\text{erg } \text{\AA}^{-1} \text{ s}^{-1} \text{ cm}^{-2}$]	σ_{flux} [$\text{erg } \text{\AA}^{-1} \text{ s}^{-1} \text{ cm}^{-2}$]	mag Vega	λ_{pivot} [\AA]
-2	929	GMOS-N	<i>g</i>	900	5	2.6×10^{-18}	7.5×10^{-19}	23.20	4729
-2	929	GMOS-N	<i>r</i>	900	5	5.2×10^{-19}	7.1×10^{-20}	24.31	6291
-2	929	GMOS-N	<i>i</i>	900	5	3.4×10^{-19}	6.1×10^{-20}	24.32	7774
-2	929	GMOS-N	<i>z</i>	1800	10	1.9×10^{-19}	3.2×10^{-20}	24.48	9695
-1	1021	GMOS-N	<i>g</i>	900	5	1.4×10^{-18}	1.7×10^{-19}	23.84	4729
-1	1021	GMOS-N	<i>r</i>	1800	10	3.2×10^{-19}	7.6×10^{-20}	24.82	6291
-1	1021	GMOS-N	<i>i</i>	1800	10	3.0×10^{-19}	6.4×10^{-20}	24.44	7774
-1	1021	GMOS-N	<i>z</i>	3600	20	1.9×10^{-19}	1.6×10^{-20}	24.46	9695
1	1125	WFC3	F438W	1998	3	7.6×10^{-19}	4.5×10^{-20}	24.85	4326
1	1125	WFC3	F555W	1848	3	6.4×10^{-19}	2.2×10^{-20}	24.47	5309
1	1125	WFC3	F600LP	4200	6	1.8×10^{-19}	8.7×10^{-21}	24.75	7506
1	1125	WFC3	F110W	1598	2	8.5×10^{-20}	4.0×10^{-21}	24.20	11 534
1	1125	WFC3	F160W	1398	2	1.7×10^{-19}	4.6×10^{-21}	22.36	15 369
2	1232	WFC3	F336W	2850	3	4.8×10^{-20}	2.9×10^{-20}	27.06	3354
2	1232	ACS	F475W	360	3	4.0×10^{-19}	4.7×10^{-20}	25.30	4744
2	1232	ACS	F625W	660	3	1.2×10^{-19}	1.9×10^{-20}	25.72	6310
2	1232	ACS	F775W	750	3	1.5×10^{-19}	1.6×10^{-20}	24.83	7693
2	1232	WFC3	F105W	965	3	4.2×10^{-20}	8.3×10^{-21}	25.28	10 552
2	1232	WFC3	F125W	828	3	7.2×10^{-20}	8.0×10^{-21}	24.07	12 486
2	1232	WFC3	F160W	828	3	1.1×10^{-19}	7.7×10^{-21}	22.78	15 369
3	1304	WFC3	F438W	2768	3	4.6×10^{-19}	3.2×10^{-20}	25.41	4326
3	1304	WFC3	F555W	3247	3	2.8×10^{-19}	1.2×10^{-20}	25.36	5309
3	1304	WFC3	F600LP	5372	6	9.4×10^{-20}	6.8×10^{-21}	25.44	7506
3	1304	WFC3	F110W	1598	2	3.9×10^{-20}	3.4×10^{-21}	25.05	11 534
3	1304	WFC3	F160W	1398	2	8.5×10^{-20}	4.0×10^{-21}	23.09	15 369
4	1403	WFC3	F438W	8000	4	3.3×10^{-19}	1.9×10^{-20}	25.75	4326
4	1403	WFC3	F555W	3880	4	2.1×10^{-19}	1.2×10^{-20}	25.67	5309
4	1403	WFC3	F600LP	5905	4	6.8×10^{-20}	5.3×10^{-21}	25.80	7506
4	1403	WFC3	F110W	1598	2	3.7×10^{-20}	3.4×10^{-21}	25.10	11 534
4	1403	WFC3	F160W	1398	2	6.9×10^{-20}	3.9×10^{-21}	23.30	15 369
5	1461	ACS	F475W	800	4	2.0×10^{-19}	3.1×10^{-20}	26.03	4744
5	1461	ACS	F625W	1600	4	$\leq 3.7 \times 10^{-20}$		≥ 26.99	6310
5	1461	ACS	F775W	2202	4	8.7×10^{-20}	9.3×10^{-21}	25.41	7693
5	1461	WFC3	F105W	1931	6	$\leq 2.8 \times 10^{-20}$		≥ 25.70	10 552
5	1461	WFC3	F125W	1587	6	4.2×10^{-20}	8.0×10^{-21}	24.66	12 486
5	1461	WFC3	F160W	1655	6	5.6×10^{-20}	7.3×10^{-21}	23.53	15 369
6	1623	WFC3	F438W	2779	3	1.7×10^{-19}	2.4×10^{-20}	26.46	4326
6	1623	WFC3	F555W	1362	3	9.9×10^{-20}	1.4×10^{-20}	26.49	5309
6	1623	WFC3	F600LP	4280	3	4.3×10^{-20}	4.3×10^{-21}	26.30	7506
6	1623	WFC3	F110W	1598	2	2.3×10^{-20}	2.8×10^{-21}	25.63	11 534
6	1623	WFC3	F160W	1398	2	3.9×10^{-20}	3.6×10^{-21}	23.92	15 369

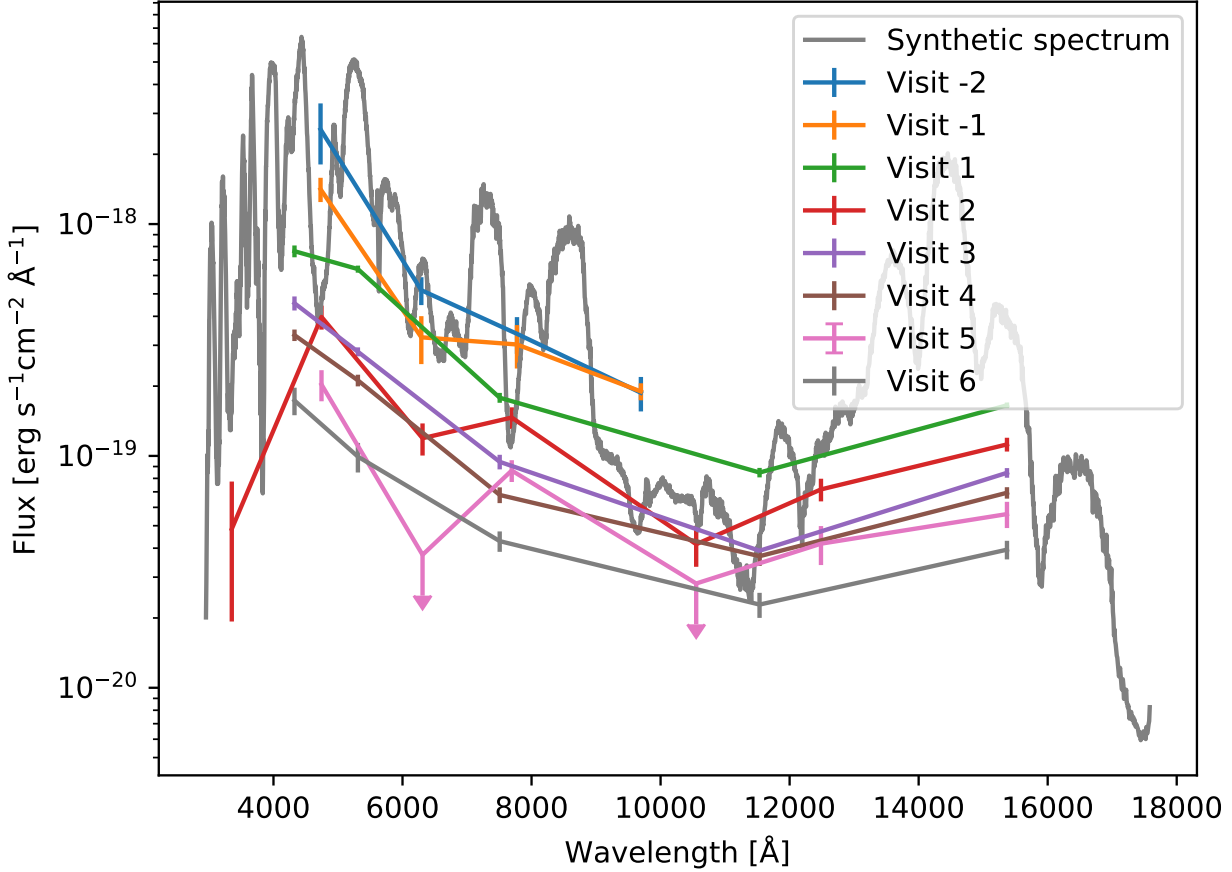


Figure 2. The lines show the measured Flux in the different bands. For a better understanding of the SED we have also added the synthetic spectrum in arbitrary flux scaling (Fransson & Jerkstrand 2015).

for our experiment. Figure 3 shows the synthetic spectrum as well as the filter sets used. We perform synthetic photometry on this synthetic spectrum using the filter curves provided by STScI⁴. An initial comparison of the synthetic spectrum with the observed flux suggests that the spectrum is a relatively good approximation for the true emission (see Figure 2). However, in the blue part of the spectrum the synthetic photometry starts to deviate.

To alleviate this deviation, we adopt the method by Dimitriadis et al. (2017) and warp the synthetic spectrum using linear interpolation between the different bands. For this purpose, we compute synthetic photometry of the synthetic spectrum and divide this with our observed photometry. We then linearly interpolate between these scalings and multiply the spectrum with this warp. This procedure is repeated until the maximum relative difference is less than

0.0001 in flux (among all bands). We estimate our uncertainties by repeating this experiment by drawing 1000 observed data points (randomly sampled using their uncertainties) and then calculate the quasi-bolometric flux measurement by integrating them. Our final integral of the warped synthetic spectrum is from 4000 Å to 16000 Å (thus excluding F336W). We believe the given process to be the optimal way to sum the flux given the unknown flux distribution and the different filter sets used at different epochs (we will discuss some implications in Section 4). The final quasi-bolometric luminosities are shown in Table 2.

3.2 Light-curve Model & Likelihood

For the model of our quasi-bolometric light curve we start by considering only radioactive decay as an energy source and assume that the energy is deposited instantaneously. Figure 4 shows the decay radiation produced by the different isotopes at late times using the abundances given in Röpke et al. (2012).

The energy input for our model is based on three decay chains

⁴ for WFC3 http://www.stsci.edu/hst/wfc3/ins_performance/throughputs/Throughput_Tables
for ACS <http://www.stsci.edu/hst/acs/analysis/throughputs/tables>

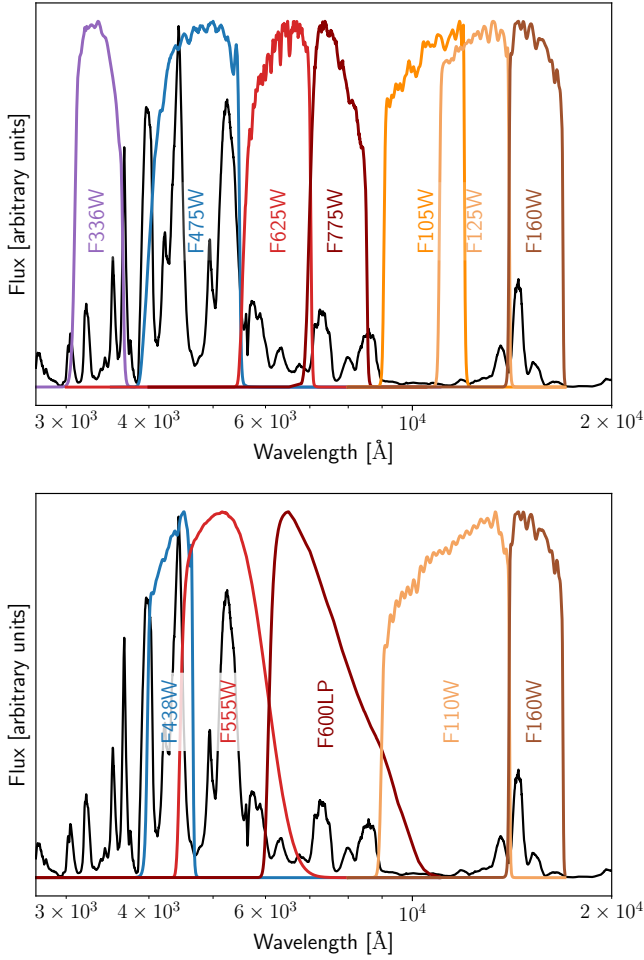
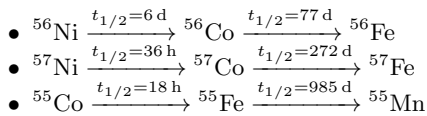


Figure 3. The figures show the synthetic spectrum by Fransson & Jerkstrand (2015) with the filter sets used by this team (top figure) and Shappee et al. (2017) (bottom figure) superimposed.

Table 2. The reconstruction of the quasi-bolometric light curve

Visit ID	t_{\max} [d]	flux density [$\text{erg s}^{-1} \text{cm}^{-2}$]	$\sigma_{\text{flux density}}$ [$\text{erg s}^{-1} \text{cm}^{-2}$]
-2	929	8.4×10^{-15}	1.4×10^{-15}
-1	1021	6.1×10^{-15}	4.6×10^{-16}
1	1125	2.8×10^{-15}	5.7×10^{-17}
2	1232	1.7×10^{-15}	9.6×10^{-17}
3	1304	1.4×10^{-15}	4.0×10^{-17}
4	1403	1.1×10^{-15}	3.3×10^{-17}
5	1461	8.4×10^{-16}	7.1×10^{-17}
6	1623	6.0×10^{-16}	3.5×10^{-17}



which produce the bulk of the energy at the epochs under consideration. For given input masses of these isotopes, we calculate the current masses using the PYNE (Scopatz et al. 2012) software package. We then calculate the decay radiation energy (data from Bhat 1998; Junde 2008; Junde et al. 2011) taking into account all electrons/positrons (beta-

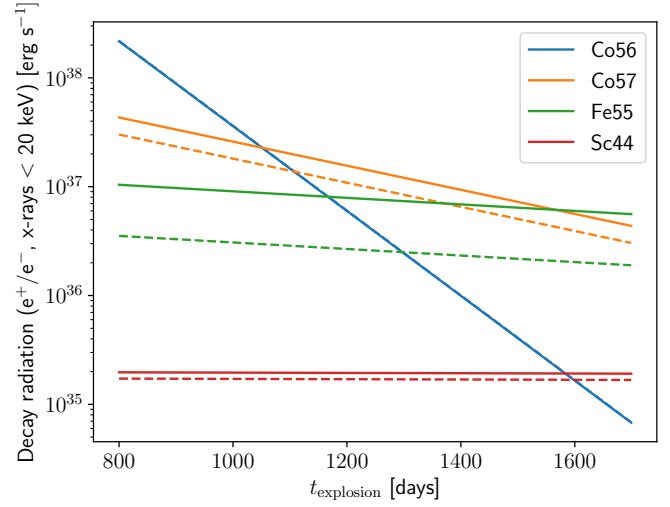


Figure 4. Decay radiation of four isotopes producing the highest energies when considering electrons/positrons and x-rays up to 20 keV. The solid lines are the N100 model. The dashed lines are the merger model.

decay, Auger and internal-conversion electrons) as well as all electromagnetic radiation up to 20 keV. We then parameterize the fraction of the decay energy that is radiated outside the observed bands and assume the rest of it is radiated within our observed window of 4000–16000 Å. Finally we scale the energy using the distance to the supernova. In total this gives five parameters (^{56}Ni , ^{57}Ni and ^{55}Co masses, the fraction outside the observed bands, and the distance).

3.3 Exploring the parameter space

We employ a Bayesian framework to explore the parameter space. Thus, we assume a Gaussian prior with $(0.5 \pm 0.1) M_{\odot}$ for ^{56}Ni from Childress et al. (2015) with a more conservative uncertainty, uniform priors of $0 - 0.1 M_{\odot}$ for ^{57}Ni and ^{55}Co , a Gaussian prior centered on 0.73 for the fraction of energy radiated outside of the observed bands falling off with a sigma of 0.1 towards a higher fraction and with a sigma of 0.3 towards a lower fraction (given a model by Fransson & Jerkstrand 2015, and capped between 0 and 1) and a prior of (6.4 ± 0.6) Mpc for the distance (Shappee & Stanek 2011). Specifically, for the fraction outside of the observed bands, we assume time independence which is likely a good assumption as the plasma state will only change extremely slowly at these very late times. Our likelihood is a simple χ^2 -likelihood that compares the generated models to the data. The parameter space is sampled using the MULTINEST (Feroz et al. 2009) algorithm and using the implementation available at <https://github.com/kbarbary/nestle>.

We present the posterior probability in Figure 5 including two confidence intervals (68%, 95%), while in Figure 6 we present all model light curves lying within the 68% confidence region.

Furthermore, we explored the sensitivity of our fit to some very simple prescriptions for the electron/positron escape and the freeze-out effect. We parametrized the freeze-out effect as an additional energy source contributing to the

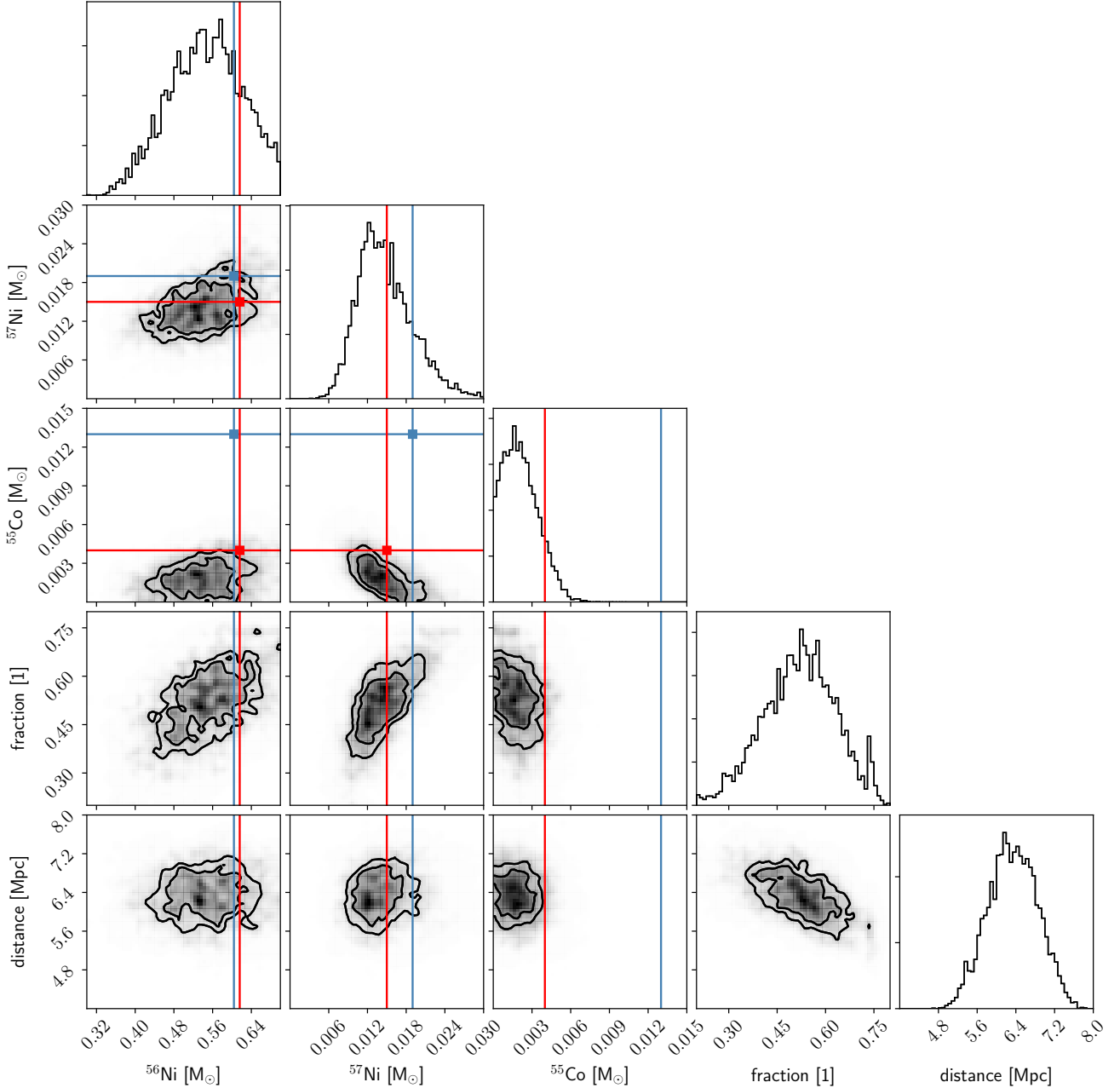


Figure 5. Corner plot of our model parameters with 68% and 95% confidence intervals (using `CORNER.PY`; Foreman-Mackey et al. 2016). The contours rely on a smoothed probability density function for better visualization. The values from Röpke et al. (2012) for the merger model have been marked in red and for the N100 model in blue (with a ^{56}Ni mass which is slightly on the high side for SN 2011fe).

late-time light curve and simply assumed this effect follows the $n_e \times n_{\text{ion}} \times V \propto t^{-3}$ relation. For the electron positron escape, we assumed a simple parametrization (escape fraction = $1 - \exp(-t/t_d)^2$) choosing $t_d = 1200 d$ (assuming a weak magnetic field in addition to that discussed in Jerkstrand 2017).

For both these effects, we focused on just finding a good fit and opted for a differential evolution algorithm to fit the appropriate parameters (isotopic masses, observed fraction, the scaling of the freeze out).

4 DISCUSSION

As discussed above, we aim to use the measured energy output, relate this to the current energy injection rate and use this to determine isotopic ratios which in turn may be used as discriminants of explosion mass and mechanism (as predicted by Röpke et al. 2012). However, in addition to the radioactive decay, there are several physical effects that if not taken into account might skew the isotopic abundance measurements (and thus any conclusions we draw). External sources of light contamination (such as compan-

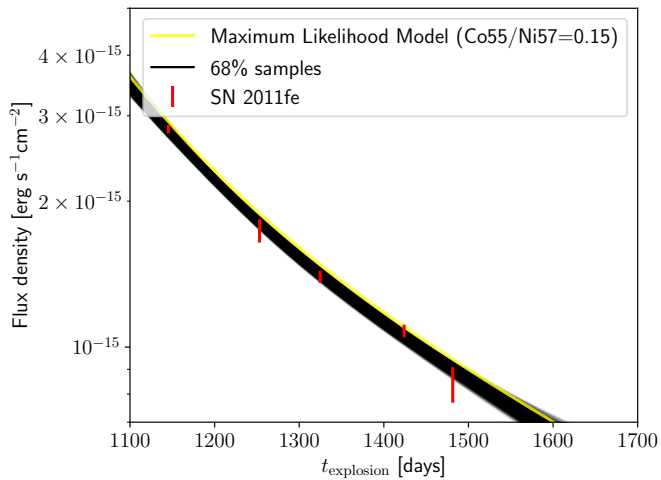


Figure 6. A fit of the radioactive model to the data. We show the maximum likelihood realization as well as all curves within the 68%-quantile.

ions, light echo, etc.) have been discussed in detail by both Shappee et al. (2017) and Dimitriadis et al. (2017).

For the internal process of converting the radioactively produced energy into observable light, Shappee et al. (2017) assume instantaneous deposition and immediate re-radiation of the radioactively produced energy. Dimitriadis et al. (2017) have also taken into account a form of parametrized escape of (electrically charged) leptons and gamma-rays (as well as hinting at potential problems due to freeze-out effects).

The uncertain magnitude of these effects results in large systematic uncertainties. Here, we will focus our discussion on some specific sources of these systematic uncertainties: 1) creation of a quasi-bolometric light curve 2) the limited wavelength range we observe 3) energy sources/sinks other than radioactive decay.

Quasi-bolometric flux Our measurements are energy output in different wavelength bands. First, we generate a derived quantity (quasi-bolometric flux) that can be compared between epochs despite the different filter sets that have been used. We construct this quasi-bolometric flux using a probable SED by Fransson & Jerkstrand (2015) which we warp slightly to reflect the mismatch when compared to the measured SED. We believe that this gives us a reliable estimate of a quasi-bolometric flux, but acknowledge that this is dependent on our choice of the synthetic spectrum (as well as the warping technique). Our experiments using simpler techniques (e.g. linear interpolation between the filters' effective wavelengths) show that they differ by a few percent (to a maximum of 8%) and thus have an effect on the overall uncertainty budget but do not dominate it.

Radiation outside the observed window Another major uncertainty comes from the fact that we only capture flux in a UVOIR window. Specifically, two factors have an important influence on the precise measurement of the isotopic abundances. The amount of the flux outside of our

observed window and more importantly if the fraction of this flux compared to the observed one is constant.

Radioactive decay in SNe Ia produces decay electrons/positrons, X-rays, and γ -rays. For the late phases considered here the ejecta are completely transparent to γ -rays, whereas lower-energy X-rays contribute. These are absorbed and produce fast electrons. This energetic electron/positron pool is supplemented by the beta decays, internal conversion and Auger electrons. Figure 5 in Fransson & Jerkstrand (2015) shows that a majority of this energy goes into the thermal pool ($> 60\%$) while the other part goes into non-thermal ionization and excitation (being shown for a pure iron plasma). This leads to an electron temperature of roughly 100 K for the outer layers and a few 100 K for the core.

The thermal pool at these late times is only able to excite fine-structure lines in the mid-/far-IR. This leads to cooling via the prominent Fe and Si lines between $20\ \mu\text{m} - 35\ \mu\text{m}$ (see Fransson & Jerkstrand 2015, for details). The presented observations are evidence that other processes must be at play to excite lines in the UVOIR bands. As discussed a non-negligible fraction of the energetic electrons/positrons do convert their energy into non-thermal excitation and ionization which is primarily radiated via UV lines. The lack of strong UV flux in epoch 2 of the observations, however, suggests that these are reprocessed (as predicted by Fransson & Jerkstrand 2015).

A simple pure radioactivity-driven model We have compared this model to the theoretical models of Röpke et al. (2012) and the measurements of Shappee et al. (2017); Dimitriadis et al. (2017) in Table 3. Our pure radioactivity based modelling gives results that are in agreement with the values presented in Shappee et al. (2017). We are not consistent with Dimitriadis et al. (2017) for the pure radioactivity model as they include additional physics (that we will also add in subsequent steps).

However, as discussed, it is unlikely that this simple radioactivity-driven model does capture all the physical processes that lead to the observed light curve. Other processes do have a significant impact on the shape of the light curve (as described in the following). Any constraints on any isotopic abundances thus carry large systematic uncertainties.

Energy sinks/sources Fransson & Jerkstrand (2015) suggest that the non-thermally excited ions might absorb a large fraction of the energy but due to the low density, the rate of recombination is slow and the release of the energy will occur much later than the injection (known as freeze-out). In effect the gas is not in ionisation equilibrium. This storage of energy will lead to a flattening of the light curve and will make any isotopic measurements using a purely radioactive decay driven model unreliable.

We use a very simple model to test how the freeze-out effect influences the already uncertain isotopic mass determinations. Figure 7 shows this effect produces a good fit even with the absence of ^{57}Ni and ^{55}Co . This result (a mimicking of the existence of ^{57}Ni) has already been discussed in Fransson & Kozma (1993) and shows how crucial a precise understanding of these late time effects is for this experiment.

Kerzendorf et al. (2014) have discussed at length the in-

	$\log_{10} {}^{56}\text{Ni}/{}^{57}\text{Ni}$	$\log_{10} {}^{56}\text{Ni}/{}^{55}\text{Co}$	$\log_{10} {}^{55}\text{Co}/{}^{57}\text{Co}$
N100 [theoretical]	1.7	1.5	0.2
merger [theoretical]	1.6	2.2	-0.6
pure radioactive (68% quantile)	1.4 - 1.9	2.0 - 5.0	-3.1 - -0.6
e ⁺ /e ⁻ escape	3	1.17	1.8
Shappee et al. 2017	1.52 - 1.65	> 2.35	< -0.7
Dimitriadis et al. 2017 (Case 2)	1.2	1.5	-0.3

Table 3. Comparison between the different measurements. Freeze-out was excluded as it only has ${}^{56}\text{Ni}$ measurement consistent with the observations, but zero for all other isotopes.

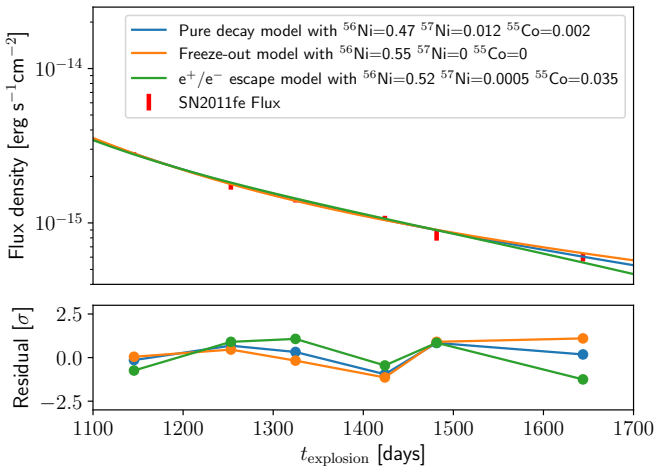


Figure 7. We show three fits to the observed quasi-bolometric flux using three distinct models: a purely radioactive decay-driven model, a model without any ${}^{57}\text{Ni}$ and ${}^{55}\text{Co}$ but with an additional prescription for freeze-out, and a model that has a time-dependent electron/positron escape fraction. All solutions are very similar (as they fit the same data) and so we plotted the fractional difference at the bottom using the radioactive model as a reference.

fluence of different magnetic field configurations on the trapping of the crucial electron/positrons (also discussed in Dimitriadis et al. 2017). A complete escape of these would lead to a sudden drop in the light curve. However, a gradual loss of a fraction of these energy carriers will subtly influence the light curve and gives an additional systematic uncertainty in the isotopic abundance determination. Figure 7 shows a very well fitting light curve with completely flipped isotopic abundances of ${}^{57}\text{Ni}$ (0.005) and ${}^{55}\text{Co}$ (0.035) compared to the maximum likelihood fit of the pure radioactivity-driven model (for the functional form refer to Section 3.3). This is consistent with Case 2 in Dimitriadis et al. (2017, see Table 3)

5 CONCLUSION

In this work we present an analysis of deep HST imaging as well as Gemini imaging at late times (900 – 1600 days) similar to Shappee et al. (2017) and Dimitriadis et al. (2017). We show that one can not draw strong conclusions from the current data due to the uncertain physical processes. For example, detailed modeling of Fransson & Jerkstrand (2015) has already shown that a simple thermal model can not ex-

plain the observed spectra (Taubenberger et al. 2015) and that the observed luminosity is likely powered by multiple effects in addition to the decay radiation.

Using such data to determine a precise isotopic abundance does require detailed modeling of the processes that shape the observables at these late times. In particular, the freeze-out effects, a possible electron/positron escape which is linked with the magnetic field configuration (see Ruiz-Lapuente & Spruit 1998) and x-ray escape will be crucial to this effort. On the observational side, we believe that a successful detection of the cooling lines in the mid-IR will further strengthen the arguments brought forth by Fransson & Jerkstrand (2015). This can likely be achieved – even at very late times – with JWST.

6 ACKNOWLEDGEMENTS

W. E. Kerzendorf was supported by an ESO Fellowship. A. J. Ruiter acknowledges funding through the Australian Research Council Centre of Excellence for All-sky Astrophysics (CAASTRO) through project number CE110001020. S. Taubenberger acknowledges support by TRR33 ‘The Dark Universe’ of the German Research Foundation (DFG). K. S. Long acknowledges support through program #13824 provided by NASA through a grant from the Space Telescope Science Institute. I. R. Seitzzahl acknowledges funding from the Australian Research Council Future Fellowship grant FT160100028. A. Jerkstrand acknowledges funding by the European Union as Framework Programme for Research and Innovation Horizon 2020 under Marie Skłodowska-Curie grant agreement No 702538.

Based in part on observations obtained at the Gemini Observatory, which is operated by the Association of Universities for Research in Astronomy, Inc., under a cooperative agreement with the NSF on behalf of the Gemini partnership: the National Science Foundation (United States), the National Research Council (Canada), CONICYT (Chile), Ministerio de Ciencia, Tecnología e Innovación Productiva (Argentina), and Ministério da Ciência, Tecnologia e Inovação (Brazil). Based also on observations made with the NASA/ESA Hubble Space Telescope, obtained at the Space Telescope Science Institute, which is operated by the Association of Universities for Research in Astronomy, Inc., under NASA contract NAS 5-26555. These observations are associated with programs #13824, #13737, and #14166.

In addition to the SW packages mentioned in the paper, we used the following software ASTROPY (Astropy Collaboration et al. 2013), NUMPY (Walt et al. 2011) SCIPY (Jones et al. 2001), PANDAS (McKinney et al. 2010), MATPLOTLIB

(Hunter 2007) and APLPY (Robitaille & Bressert 2012) to analyze and visualize the data.

Finally, we would like to thank the anonymous referee and Ben Shappee for suggestions that did improve the paper.

REFERENCES

- Aihara H., et al., 2011, *ApJS*, 193, 29
 Astropy Collaboration et al., 2013, *A&A*, 558, A33
 Axelrod T. S., 1980, PhD thesis, California Univ., Santa Cruz.
 Bertin E., Mellier Y., Radovich M., Missonnier G., Didelon P., Morin B., 2002, in Bohlender D. A., Durand D., Handley T. H., eds, *Astronomical Society of the Pacific Conference Series Vol. 281, Astronomical Data Analysis Software and Systems XI*. p. 228
 Bhat M. R., 1998, *Nuclear Data Sheets*, 85, 415
 Chan K.-W., Lingenfelter R. E., 1993, *ApJ*, 405, 614
 Chiaberge M., Lim P. L., Kozhurina-Platais V., Sirianni M., Mack J., 2009, Technical report, Updated CTE photometric correction for WFC and HRC
 Childress M. J., et al., 2015, *MNRAS*, 454, 3816
 Colgate S. A., McKee C., 1969, *ApJ*, 157, 623
 Dimitriadis G., et al., 2017, *MNRAS*, 468, 3798
 Dolphin A. E., 2000, *PASP*, 112, 1383
 Feroz F., Hobson M. P., Bridges M., 2009, *MNRAS*, 398, 1601
 Foreman-Mackey D., et al., 2016, *corner.py: corner.py v2.0.0*, doi:10.5281/zenodo.53155, <https://doi.org/10.5281/zenodo.53155>
 Fransson C., Jerkstrand A., 2015, *ApJ*, 814, L2
 Fransson C., Kozma C., 1993, *ApJ*, 408, L25
 Fukugita M., Ichikawa T., Gunn J. E., Doi M., Shimasaku K., Schneider D. P., 1996, *AJ*, 111, 1748
 Gonzaga S., et al. 2012, *The DrizzlePac Handbook*
 Graur O., Zurek D., Shara M. M., Riess A. G., Seitzmann I. R., Rest A., 2016, *ApJ*, 819, 31
 Hook I. M., Jørgensen I., Allington-Smith J. R., Davies R. L., Metcalfe N., Murowinski R. G., Crampton D., 2004, *PASP*, 116, 425
 Hunter J. D., 2007, *Computing In Science & Engineering*, 9, 90
 Jerkstrand A., 2017, preprint, ([arXiv:1702.06702](https://arxiv.org/abs/1702.06702))
 Jones E., Oliphant T., Peterson P., et al., 2001, *SciPy: Open source scientific tools for Python*, <http://www.scipy.org/>
 Junde H., 2008, *Nuclear Data Sheets*, 109, 787
 Junde H., Su H., Dong Y., 2011, *Nuclear Data Sheets*, 112, 1513
 Kerzendorf W. E., Taubenberger S., Seitzmann I. R., Ruiter A. J., 2014, *ApJ*, 796, L26
 Leloudas G., et al., 2009, *A&A*, 505, 265
 McKinney W., et al., 2010, in *Proceedings of the 9th Python in Science Conference*. pp 51–56
 Milne P. A., The L.-S., Leising M. D., 1999, *ApJS*, 124, 503
 Milne P. A., The L.-S., Leising M. D., 2001, *ApJ*, 559, 1019
 Patat F., et al., 2013, *A&A*, 549, A62
 Pereira R., et al., 2013, *A&A*, 554, A27
 Robitaille T., Bressert E., 2012, *APLpy: Astronomical Plotting Library in Python, Astrophysics Source Code Library* (ascl:1208.017)
 Röpke F. K., et al., 2012, *ApJ*, 750, L19
 Ruiz-Lapuente P., Spruit H. C., 1998, *ApJ*, 500, 360
 Scopatz A., Romano P., Wilson P., Slaybaugh R., Huff K., Relson E., 2012, in *SciPy 2012*. Austin, TX, USA
 Seitzmann I. R., 2011, *Progress in Particle and Nuclear Physics*, 66, 329
 Seitzmann I. R., Taubenberger S., Sim S. A., 2009, *MNRAS*, 400, 531
 Shappee B. J., Stanek K. Z., 2011, *ApJ*, 733, 124
 Shappee B. J., Stanek K. Z., Kochanek C. S., Gerke J. R., Garnavich P., 2015, *The Astronomer's Telegram*, 7392
 Shappee B. J., Stanek K. Z., Kochanek C. S., Garnavich P. M., 2017, *ApJ*, 841, 48
 Sollerman J., et al., 2004, *A&A*, 428, 555
 Spyromilio J., Graham J. R., 1992, *MNRAS*, 255, 671
 Stritzinger M., Sollerman J., 2007, *A&A*, 470, L1
 Taubenberger S., et al., 2015, *MNRAS*, 448, L48
 Walt S. v. d., Colbert S. C., Varoquaux G., 2011, *Computing in Science & Engineering*, 13, 22
 Yang Y., et al., 2017, preprint, ([arXiv:1704.01431](https://arxiv.org/abs/1704.01431))
 van Dokkum P. G., 2001, *PASP*, 113, 1420